Microwave-Induced Thermoacoustic Imaging of Subcutaneous Vasculature With Near-Field RF Excitation

Miaad S. Aliroteh, *Student Member, IEEE*, and Amin Arbabian, *Member, IEEE*

***Abstract*— Imaging of subcutaneous vasculature is of great interest for biometric security and point-of-care medicine. We investigate the feasibility of microwave-induced thermoacoustic (TA) tomography as a safe, compact, low-power, and cost-effective imaging technique for subcutaneous vasculature by means of application-specific design of near-field, radio frequency (RF) applicators. Using commercial transducers, we demonstrate proof-of-concept TA imaging of synthetic phantoms, plant vasculature, and earthworm blood vessels with only 50 W of peak power, or 42 mW average power, at 300 μm resolution. The proposed RF applicator design enabled uniform, orientation-independent illumination of vasculature phantoms with only 10% variation. Finally, we show that the benefits of microwave contrast make possible the distinction of actual blood vessels, in an earthworm, from surrounding tissue within a modest receiver dynamic range of 40 dB.**

***Index Terms*— Biomedical imaging, biometrics, microwave imaging, near field, photoacoustic (PA) effect, radio frequency (RF) applicator, thermoacoustic (TA) imaging, ultrasonic imaging, ultrasound (US).**

I. Introduction

With the advent of the Internet of Things and the expansion of personal and sensitive data onto the cloud, security and authentication have become a growing challenge. A potential solution may be biometric authentication via 3-D imaging of subcutaneous vasculature [1]–[3], residing less than 3 mm below the skin in the fingertips, in a noninvasive, convenient, and economically scalable manner, using an all-electronic and portable platform. Subcutaneous features, such as blood vessels, are more difficult to replicate than superficial biometric features, such as fingerprints, whose spoofing is possible with technologies, such as 3-D printing, stereolithography, and conductive inks [4]. An integrated vasculature imaging system on a miniature printed circuit board (PCB) is the ideal form factor for this kind of technology, as it can be embedded in a variety of end applications, including automobiles, home security, banking systems, airport terminals, and of course, mobile phones and wearable electronics.

Manuscript received February 24, 2017; revised May 15, 2017; accepted June 2, 2017. Date of publication June 30, 2017; date of current version January 4, 2018. This work was supported in part by the Qualcomm Innovation Fellowship Program, in part by the Texas Instruments University Relations Program, and in part by the Stanford System-X Alliance. *(Corresponding author: Miaad S. Aliroteh.)*

The authors are with the Department of Electrical Engineering, Stanford University, Stanford, CA 94305 USA (e-mail: miaad@stanford.edu).

Color versions of one or more of the figures in this paper are available online at http://ieeexplore.ieee.org.

Digital Object Identifier 10.1109/TMTT.2017.2714664

Conventional clinical angiography techniques for imaging of vasculature include digital subtraction angiography (DSA), magnetic resonance angiography, computed tomography angiography (CTA), and conventional ultrasound (US) [5]. In addition to the use of hazardous contrast agents or radiation, as is the case in DSA and CTA, the large size of these imaging devices prevents their direct application to biometric authentication. Similarly, the inherently low contrast of US necessitates the use of more expensive and high-dynamic range electronics, commonly employed in larger clinical devices, or the injection of contrast agents [6], [7]. Other techniques include Doppler optical coherence tomography (DOCT) [2], [3], [8] and optical IR imaging [1]. DOCT has demonstrated high-quality vascular images in the retina, yet penetration of the skin remains a challenge. Optical IR imaging can only generate 2-D projections of vasculature and, like most optical sensing platforms (including DOCT), has limited short-term potential for integration with electronics due to optical requirements.

Another interesting approach is multimodal imaging, which includes photoacoustic (PA) imaging [9]–[25] and microwave-induced thermoacoustic (TA) imaging [26]–[45]. Both of these techniques operate by modulated heating of the sample within safe levels in order to generate acoustic waves by means of thermal expansion. This effect was first demonstrated by Alexander Graham Bell in 1880, when he used a pulsed light source to generate weak acoustic waves [9]. Over time, this evolved into PA imaging, which has been used to capture high-quality images of vasculature, including that within the finger, using pulsed or continuous-wave (CW) laser sources [10]–[25]. Motivated by development of a low-cost and portable imaging tool for diagnostics and screening, TA was proposed soon after PA for improved penetration depth by replacing the laser excitation with microwave heating [28].

TA imaging uses radio frequency (RF) excitation for high-contrast and ultrasonic detection to obtain high resolution with only modest signal bandwidth. In principle, both excitation (transmit) and detection (receive) can be achieved using all-electronic devices by leveraging modern RF and micro-electromechanical system (MEMS) technologies that have undergone many waves of evolution in the communication and cellular phone industries. While conventional TA implementations require kilowatts to megawatts of peak microwave power—obtainable only with high-power vacuum tubes, spark gaps, or transmission line pulsers—TA imaging of excised organs, such as the kidney and prostate, has shown the great

potential of TA as an alternative imaging modality [26]–[29], [31]–[33], [43].

In addition to scalability limitations due to optical requirements, concerns of eye safety are an obstacle for a consumer-grade PA imaging system. Indeed, most PA imaging systems in the literature, such as [2], are focused on controlled clinical environments, where safety glasses or protective curtains are used to ensure laser exposure below the recommended limits of about 1 μJ/cm^2 per pulse or 5 mW/cm^2 in CW as specified by institutions, such as ANSI. This is in contrast to the much higher limits, about 20 mJ/cm^2 per pulse or 200 mW/cm^2 in CW, set to ensure safe levels of specific absorption rate (SAR) within the skin and tissue under examination [10]–[12], [14]–[21]. This is attributed to the focusing of visible and near-infrared light on the retina. TA imaging can potentially integrate the safety mechanism by RF focusing in the near field and quasi-near field in order to mitigate far-field exposure of radiation to address eye safety and minimize radio spectrum pollution. Thus, TA imaging of the fingertips is mainly limited by the near-field SAR guideline of about 2 W/kg averaged over 10 g in 6 min for CW and 2 mJ over 10 g for pulsed microwave excitation, taken conservatively between institutions, such as IEC, FDA, and ICNIRP [46]. Back-of-the-envelope calculations show that most TA imaging systems can meet these safety limits as verified by [36].

New directions of research in TA imaging include noncontact sensing [39]–[42], novel applicator designs and beamforming [37], [43]–[45], [47], new image reconstruction and processing techniques [48]–[50], as well as CW techniques [34]–[37] for peak power reduction. Our work in [47], however, is most relevant here, as it introduced the idea of low-power, pulsed TA imaging systems specifically designed for shallow penetration depths, and suitable for imaging subcutaneous vasculature. In [47], we demonstrated the potential of this concept by means of phantoms and simple plant vasculature, and highlighted applications requiring a high-contrast, low-cost, easy-to-maintain, and intuitive point-of-care diagnostic imaging tool. This paper extends our prior work by presenting a detailed design methodology and analysis of the proposed TA system, and also extends that work with new experiments involving imaging of phantoms with complex vascular structures and earthworms for a more realistic assessment of this concept. Our results and achieved performance indicate that this technique could also be applicable to biometrics after further development envisioned in Fig. 1. In particular, we investigate the design of TA RF applicators that are customized for low-power, near-field, and quasi-near-field performance instead of conventional far-field microwave antennas intended for radiation into tissue, including those in [37] and [51]. By limiting electromagnetic fields to this regime, we forfeit superfluous penetration depth in order to reduce peak power requirements.

In this paper, organized into six major sections, we demonstrate the feasibility of a consumer-grade, all-electronic, biometric imaging system based on TA, as conceptualized in Fig. 1, using proof-of-concept experimental data and analysis of electromagnetic simulations. In Section II, we provide

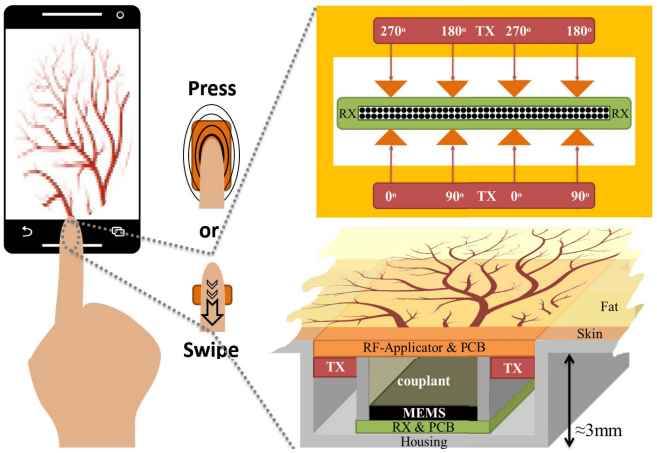

Fig. 1. Concept of compact and low-power TA imaging of subcutaneous vasculature for biometrics, employing custom MEMS US transducers and mainstream receiver (RX) electronics. The multiphase RF transmitter (TX) may time-share existing hardware, such as phone's RF power amplifiers.

system specifications for the concept in Fig. 1. Next, in Section III, we introduce essential theoretical concepts relating to TA physics, acoustic noise, receiver arrays (including scanning techniques), and heuristics for RF-applicator design. Subsequently, in Sections IV and V, we highlight some proof-of-concept experimental results obtained with two different receiver scanning approaches. Finally, in Section VI, we combine experimental data, simulations, and theory to demonstrate the feasibility of TA imaging for consumer-grade biometric authentication.

II. Specifications

The specification for a TA biometric imaging system in Fig. 1 can be outlined with the goal of capturing fingertip vasculature between 150 μm to 1 mm thick, which resides between 0.5 and 3 mm beneath the surface of the skin [2], [3], [15]. To represent this information, a postprocessed image would require one or more bits of data, per pixel, approximately equivalent to a signal-to-noise ratio (SNR) of 8 dB or more [52]. To account for up to 20% variations in RF excitation, an additional 2 dB is required for a total SNR of 10 dB or more, which is consistent with experimental observations. The TA imaging system must also provide sufficient contrast between vasculature and surrounding tissue with low dynamic range (<60 dB) receiver electronics to enable simple and low-cost signal acquisition circuitry. Finally, practicality and safety dictate that the image acquisition time should be limited to a few seconds, during which the power consumption must be restricted to a level manageable with portable consumer electronics [53].

III. Theory

A. Thermoacoustic Waves

In both PA and TA, the production and propagation of pressure waves due to thermoelastic expansion are governed

by the nonhomogeneous wave equation

$$\left(\nabla^2 - \frac{1}{v^2}\frac{\partial^2}{\partial t^2}\right) p(r,t) = -\frac{\beta}{C}\frac{\partial Q(r,t)}{\partial t}. \quad (1)$$

Here, the heating function, $Q(r,t)$, defined as the absorbed thermal energy density per unit time, is related to the generated stress, $p(r,t)$, at position r and time t, through the thermal-expansion coefficient, β, and the specific heat capacity, C, of the medium. The stress propagates at the speed of sound, v, governed by the wave equation, whose solutions for slab, cylindrical, and spherical geometries under short and long pulsed laser excitation are detailed in [24] and [25]. These results can be applied to TA by appropriately modeling the heat function, which is proportional to the electromagnetic loss and, hence, quadratically related to the root mean square of the electric field, $E(r,t)$, as [36]

$$Q(r,t) = [\sigma(f) + 2\pi f \cdot \epsilon''(f)] \cdot |E(r,t)|^2. \quad (2)$$

Here, the material conductivity, $\sigma(f)$, and complex permittivity, $\epsilon''(f)$, contribute to the losses and may depend on the operating microwave frequency, f. Finally, our proof-of-concept TA experiments use mineral oil as a convenient, electrically neutral acoustic couplant.

B. RF-Applicator Design

As observable from (2), the strength of the generated acoustic signal is determined by the amount of absorption, which is related to the electric field strength in the desired tissue (here the superficial blood vessels), and increases with operating frequency (when variations in dielectric properties are negligible). Most TA imaging works in the literature, however, operate up to only several gigahertz, since the design complexity and the cost of RF power amplifiers also scale with frequency [26]–[42]. In this section, we will review the advantages and limitations of the conventional, open-face waveguide, excitation scheme for the application envisioned in Fig. 1, the proposal of a new RF applicator in the near field, abstractions for analysis and design of this RF applicator, verification with simulations, and finally a brief comparison with other candidates.

Conventional TA imaging systems use an open-face waveguide to deliver RF excitation with propagating plane waves, similar to Fig. 2, where it is applied to a simplified model of skin, fat, and superficial vasculature. In order to overcome the impedance mismatch at the skin and maximize the amount of power delivery, the potential operating frequency regime would be where the skin thickness is either around half wavelength (e.g., 24 GHz for 1-mm-thick skin) or much smaller than the wavelength (e.g., $\leqslant$5 GHz for 1-mm skin $\leqslant \lambda/10$). As discussed earlier, lower frequency regime is preferable due to availability of amplifiers with sufficient peak power and efficiency. It is also crucial that the electric fields are approximately tangential to the fat–blood interface, as in Fig. 2, in order to maintain continuity of the electric field strength as the wave propagates from the low-permittivity fat medium into the high-permittivity blood medium. The drawbacks of this approach include unused, excess radiation

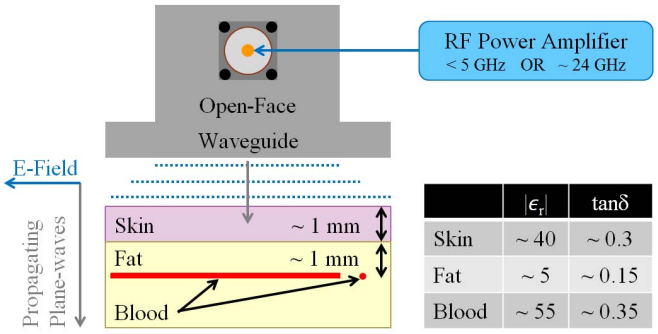

Fig. 2. Conventional TA imaging setup using plane-wave excitation with an open-face waveguide and a simplified tissue model of superficial vasculature, with relative permittivity, ϵ_r, and loss tangent, $\tan\delta$, tabulated.

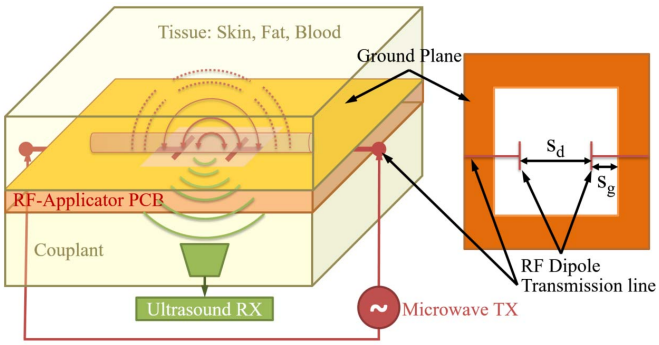

Fig. 3. General design of the dipole RF applicator and its key parameters s_d and s_g. The microwave transmitter feeds the dipole electrodes through transmission lines, shielded between ground planes, where controlled exposure to tissue results in energy absorption, microheating, thermal expansion, and production of US that is captured by the receiver chain.

beyond the blood layer and the impracticallity of constructing a compact system, like that in Fig. 1, from bulky waveguides.

To address these limitations, we must deliver RF excitation with a thin and planar structure, such as a PCB and maximized microwave absorption in blood, by generating approximately tangential electric fields at the fat–blood interface, while operating at lower microwave frequencies. One approach is to use the PCB structure in Fig. 3 operating in the near-field regime. Here, two transmission lines feed RF power into two electrodes that are within the internal layer of the PCB. The PCB is in direct contact with skin and a few millimeters from superficial vasculature. In addition to tangential electric fields along the x-axis, it is desirable to use additional dipoles to generate tangential electric fields along the y-axis, similar to Fig. 4(a). This enables more uniform illumination of blood vessels independent of their orientation.

In order to analyze this complex problem, we will make use of simplifying abstractions and approximations together with full-wave simulations similar to approaches used in [54]–[57]. Consider the electrostatic dipole abstraction in Fig. 4(c). The static electric field along the dipole center, described by

$$E_x = \frac{q}{4\pi\epsilon}\left(\frac{-s_d}{\sqrt{h^2 + \frac{s_d^2}{4}}^3}\right) \quad (3)$$

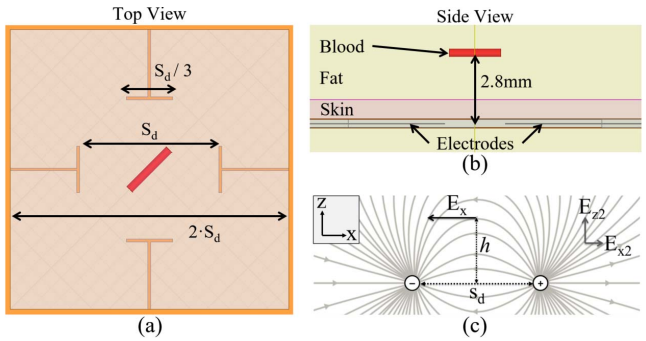

Fig. 4. (a) Top view and (b) side view of the simulation setup and simplified tissue model with key dimensions of the design as a function of electrode spacing, s_d. (c) Electrostatic dipole abstraction approximates the quasi-static electric field from a pair of RF electrodes in the near-field region.

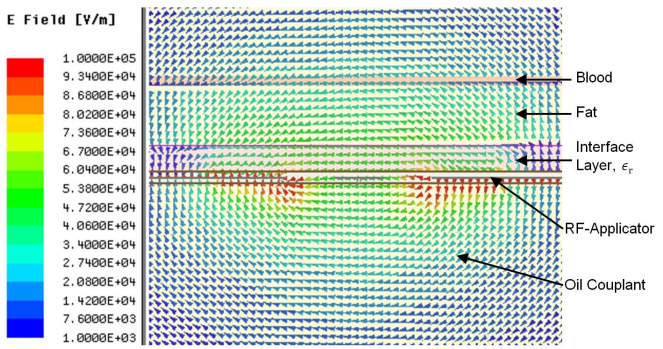

Fig. 6. Simulated electric field pattern for an elongated blood vessel within a layered fat and skin tissue model is similar to the pattern predicted by the simplified abstraction.

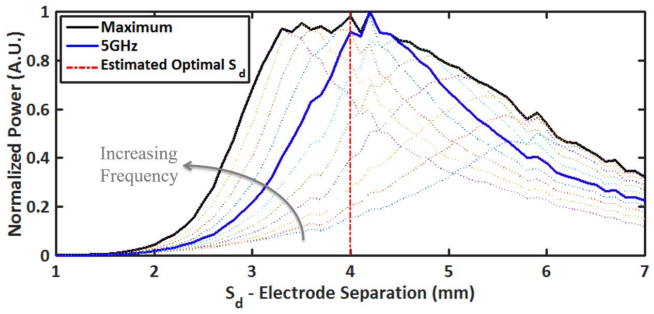

Fig. 5. Simulated, normalized absorbed power in blood for Fig. 4(a). Estimates of optimal frequency and electrode separation of 5.4 GHz and 4 mm based on (4) and (5) are similar to simulation results. The curve corresponding to the 5 GHz optimal operating frequency is highlighted as well as the overall maximum absorption in blood across 3.5–6 GHz.

can be maximized for a given standoff from the dipole, h, by choosing the dipole separation, s_d, as

$$s_d = \sqrt{2}h. \tag{4}$$

Practical RF applicators will inevitably be electrodynamic variations of Fig. 4(c), and only approximated by (3) under the assumption of near-field operation. This approximation begins to break down as the operating frequency increases and a transition is made from the near-field regime into the far-field regime, where s_d is larger than the wavelength. This transition occurs after the optimal frequency, which roughly corresponds to a wavelength twice the electrode separation, s_d, in a medium with a relative dielectric constant, ϵ_r, averaged between skin and blood. With the speed of light, c, this can be written as

$$f \approx \frac{c}{\sqrt{\epsilon_r}} \frac{1}{2 \cdot s_d}. \tag{5}$$

The abstractions in (4) and (5) serve as a heuristic approximation for the proposed RF applicator in Figs. 3 and 4. In the following ANSYS HFSS full-wave simulations, shown in Fig. 5, we verify the utility of (4) and (5) in obtaining the first-order estimates of optimal electrode spacing and operating frequency. The simplified model of Fig. 4(b) consists of a layer of skin, fat, and a blood vessel segment, 0.3 mm in diameter, located 2.8 mm away from the electrodes, beneath the skin. The frequency-dependent dielectric properties of this tissue are modeled based on collected data by [58]. An optimal electrode separation of 4 mm and a frequency of 5.4 GHz are predicted by (4) and (5). This configuration is simulated for a range of electrode separation, s_d, from 1 to 7 mm in 0.1-mm increments with the normalized power absorbed in blood shown in Fig. 5 for a range of frequencies, between 3.5 and 6 GHz in 0.25 GHz steps. A peak near 4.2 mm is observed at the optimal operating frequency of 5 GHz, which is in good agreement with the initial values from (4) and (5). The loss tangent of blood and skin increases with frequency, in the 3–30 GHz range, but that of skin increases faster based on data from [58]. So it is expected that the absorbed power in blood will increase with frequency up to a point at which increases in skin absorption dominate as observed in Fig. 5.

Simulations demonstrate that the electric field pattern, shown in Fig. 6, is close to the approximation in Fig. 4(c) for frequencies corresponding to the near-field regime, approximately <6 GHz. At the PCB–skin interface, most of the electric field is normal to the interface and is reduced in skin due to its large permittivity. The tangential component of the electric field is continuous, resulting in a weaker total electric field, parallel with the skin. This is favorable as it lowers losses in skin and maintains an electric field below the 10^5 V/m safe limit [46]. At the skin–fat interface, the situation is reversed, with the normal component increasing due to fat's low permittivity, resulting in a total electric field pattern similar to the estimation in Fig. 4(c). Consequently, at the blood–fat interface, the electric field is mostly tangential and its continuity ensures that the enhanced field in the fat is transferred into blood as desired. It is interesting to note that with the simplified tissue geometry, this effect from the skin layer's higher permittivity compensates for skin absorption losses, resulting in electric fields in blood that are about 1.4× larger, at the optimal frequency of 5 GHz, than if the skin layer was replaced with fat. Thus, in the near field, it is actually desirable to have an electric field that starts normal to the skin layer and later becomes tangential at the blood, as is inherent to the proposed RF applicator.

Finally, we will briefly explore other RF-applicator designs, shown in Fig. 7, that we investigated for our target application. In Fig. 7(a), the finger is sandwiched between two parallel

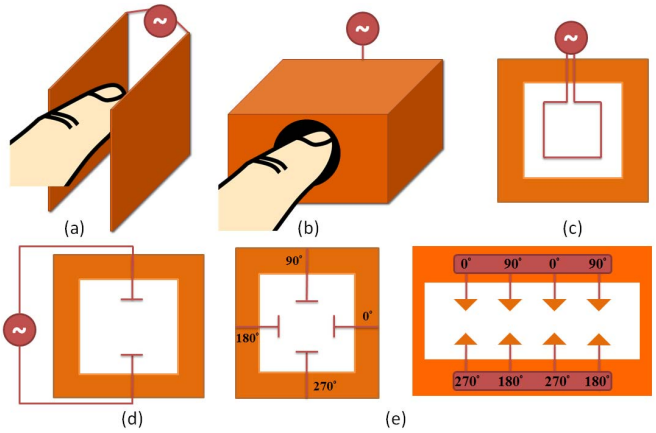

Fig. 7. Various RF-applicator designs that were (a), (b) tested in simulation as well as (c), (d), and (e) with experiments. Designs (a), (c) yielded poor performance, (b) resulted in impractical dimensions, and (e) achieved the best performance with minimal size.

plate electrodes, which operate at low frequencies. Here, the electric field is normal to the blood–fat interface leading to unfavorably low field strengths in the blood. In Fig. 7(b), a resonant cavity had good performance in simulation but it is bulky for the envisioned application. Simulations show that the absorption mechanism of the loop RF applicator in Fig. 7(c) is through the electric field as the magnetic losses in tissue were negligible. This applicator was also constructed and tested, and unfortunately, the large currents present in the loop produce self-heating and parasitic TA signals that are undesired. The dipole RF applicator in Fig. 7(d) was already discussed, analyzed, and does not suffer from excessive currents. Finally, we investigated the possibility of extending the dipole RF applicator into multiple dipoles as in Fig. 7(e). This allows using of multiple polarizations to increase illumination uniformity as discussed in more detail in Section V-C.

C. Transducer and Acoustic Noise

Thermal noise manifests in mechanical and acoustic systems as the random motion of particles and structures. For an US transducer, this can be captured by

$$p_n = \sqrt{kT\left(1+\frac{1}{\eta_{\text{eff}}}\right)Z/A} \tag{6}$$

as a pressure noise density with units of [Pa/$\sqrt{\text{Hz}}$] [12]. Here, k is Boltzmann's constant, T is the temperature, Z is the medium's acoustic impedance, A is the sensor area, and η_{eff} is its effective efficiency. The acoustic inefficiencies and losses in the transducer can contribute significant excess noise resulting in a larger noise equivalent pressure (NEP). The transducer efficiency is related to its insertion loss (IL), which can be calculated by

$$\text{IL} = \frac{1}{\eta_{\text{eff}}} = \sqrt{\frac{V_{\text{RX}}}{V_{\text{TX}}}}. \tag{7}$$

Here, a pulse-echo experiment is performed, where the transducer is excited with a short transmit pulse, at a voltage of V_{TX}, after which the subsequent echo signal, V_{RX}, is captured. It is assumed that the experimental setup would ensure near total reflection of the transmitted wave with negligible acoustic loss due to propagation and defraction, or account for these losses in postprocessing.

The Olympus Panametric V320 device used in this paper serves as an example of a typical commercial piezotransducer. This device has a 26 dB IL, which represents about 20× increase of the noise floor from the level dictated by thermodynamics, even prior to considerations of noise from receive electronics. In contrast, MEMS US transducers in the form of capacitive micromachined US transducers (CMUTs) have demonstrated lower IL, reaching down to 3 dB [59]. Although these devices are not yet widely available, their commercialization is an emerging trend [60], [61].

D. Transducer Arrays and Scanning

The ideal TA system in Fig. 1 consists of a CMUT phased array in order to achieve high-speed and high-resolution imaging in a compact form factor. The depth resolution, Δr, for a microwave excitation pulse of duration Δt is given by

$$\Delta r = v\Delta t \approx \frac{1.2\cdot v}{\text{BW}_{-6\,\text{dB}}} \approx \lambda_{\text{min}} \tag{8}$$

where Δt is approximately limited by the −6 dB acoustic bandwidth, $\text{BW}_{-6\,\text{dB}}$. For a relatively wideband transducer, Δr is approximately equal to the minimum acoustics wavelength, λ_{min}. The wavelength and transducer diameter, D, also determine the acoustic beam angle, θ, measured from its 0 dB beam centerline to its −6 dB beam edge, through the reception directivity function [62]. This can be simplified to

$$\theta \approx \arcsin\left(\frac{0.7\lambda}{D}\right) \overset{D\gg\lambda}{\approx} \frac{0.7\lambda}{D} \tag{9}$$

for a circular aperature. This, in turn, determines the phased array's maximum useful synthetic aperture size, $L_{\text{synth}}(R)$, at given range, R, which establishes the lateral resolution, Δl, as calculated by [62]

$$\Delta l = \frac{\lambda}{L_{\text{synth}}(R)}R = \frac{\lambda}{2\tan(\theta)} \overset{D\gg\lambda}{\approx} \frac{D}{1.4}. \tag{10}$$

Reducing the element size and pitch improves the lateral resolution while it also increases the per-element noise floor, since the area term in (6) is reduced as a consequence. This analysis is similar to that in [63] for millimeter-wave imaging except that here we are not aperature-size limited, due to the close proximity of the blood vessels to the transducer array in Fig. 1.

Although (6)–(10) inform the first-order transducer array design for imaging applications, we start by scanning single-element transducers as a proxy to obtain proof-of-concept measurements. In particular, scanning a single, commercially available, transducer over a circular aperture, as shown in Fig. 8, can be used to obtain good lateral and depth resolution, both of which can be approximated by (8). In this case, however, the distance between the target and the transducer is significantly larger (>50 mm), and with the frequency-dependent viscous attenuation of the mineral oil couplant, this can artificially limit the effective acoustic bandwidth and,

Fig. 8. Circular scanning of a bulky, off-the-shelf transducer using a motorized stage, together with a simple dipole RF applicator, can result in high-resolution TA cross-sectional images [47].

hence, resolution. For example, the transducer used in this paper has a baseline $BW_{-6\,dB}$ beyond 12 MHz; however, its effective $BW_{-6\,dB}$ was limited to 6 MHz in mineral oil, corresponding to a depth resolution of approximately 300 μm.

While the circular scanning approach can obtain high-quality cross-sectional images, such as those demonstrated by [15]–[17] using PA, this technique is not directly applicable in the desired form factor shown in Fig. 1. A more direct approach is to perform 2-D raster scanning with a single transducer as a means of producing a synthetic phased-array system. Ideally, this should be accomplished using a single-element CMUT with similar dimensions and characteristics of an element within the array of Fig. 1. In the absence of such a CMUT device, a commercial focused transducer can serve as a substitute, as done in [18] for PA imaging. However, the lateral resolution will be twice the beamwidth at the focal point, which for off-the-shelf devices is usually larger than the bandwidth-limited range resolution. Thus, circular scanning obtains better overall image resolution as it relies mainly on range resolution for image reconstruction. In this paper, we use both circular and raster scanning of commercial transducers in order to indirectly assess and predict the performance of the ideal CMUT-array enabled system proposed in Fig. 1.

IV. Circular Scanning and Results

To demonstrate the feasibility of the proposed system in Fig. 1, we start by circularly scanning commercial, single-element transducers as a proxy to obtain proof-of-concept measurements. With this approach, we will demonstrate TA imaging results that satisfy many of the required specifications, resolution in particular, using an RF applicator based on a simple dipole design, and later, we will look at the raster scanning approach. Both approaches use a common experimental setup consisting of the transmit (TX) and receive (RX) chains as in Fig. 9. The TX chain begins at the function generator, which produces the envelope signal: a 167 ns pulse with 5 kHz repetition rate. This envelope signal modulates the 2 GHz carrier produced by the signal generator, which then feeds the preamplifier, the solid-state power amplifier, and the circulator. An RG400 coaxial transmission line feeds the circulator output, limited to 50 W_{pk} or 71 V_{pk} corresponding to 42 mW_{avg}, into the RF applicator.

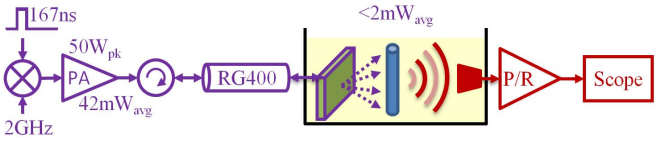

Fig. 9. Experimental setup: the sample is submerged in oil, together with the RF applicator, where it absorbs less than 2 mW_{avg} to produce US waves from microwave-induced thermal expansion similar to [47].

A. Experimental Setup

The experimental setup for the circular scanning approach used a small excitation PCB, made with RO-3003 substrate, consisting of two gold-plated copper traces spaced 4 mm apart, as shown in Fig. 8. Submerged inside mineral oil for acoustic coupling, as shown in Fig. 9, the sample is placed near the RF applicator for electromagnetic excitation and approximately 63 mm away from the US transducer (Olympus Panametric V320). The transducer is connected to the RX chain: a commercial front end in the form of a 60 dB pulser/reciever amplifier, whose output is captured by the oscilloscope at 100 MS/s using a 20 MHz bandwidth and 500–8192 averages. Motorized rotation stages perform 360° circular scanning in 1° steps. Reconstruction is performed in MATLAB by solving the 2D acoustic wave equation under time reversal using the k-Wave toolbox [64].

B. Dipole RF Applicator

In order to facilitate circular-scan TA imaging for early proof-of-concept experiments, a compact two-trace excitation PCB, the dipole RF applicator, was designed with a simple single-phase RF input port, as shown in Fig. 8. According to (4), the trace spacing of 4 mm is ideal for a penetration depth of 3 mm, which is suitable for the application. These traces are about a quarter-wavelength long in mineral oil. Additional traces form a transmission line that route RF power, similar to a twin-lead cable. Using a water medium would increase absorption by the couplant; however, this is less significant in our application, as the sample is situated adjacent to the RF applicator and only a few millimeters of penetration are required to reach the blood vessels of interest. Nonetheless, the higher dielectric constant significantly reduces the wavelength, which is undesirable, as this alters the characteristic impedance of transmission lines, causing an increase of reflected power, as well as making the two electrodes traces behave more as ill-controlled antennae. Obviously, this is an artifact of the simplified dipole RF-applicator implementation in Fig. 8, which is resolved when the transmission lines are shielded between ground planes within the internal layers of the PCB as proposed in Fig. 3. Normally, the termination of the electrodes will be open, which generates standing waves that result in the maximum electric field intensity at the termination. When the imaging sample is placed near the termination, this behavior can be maintained if the sample is relatively small, so that a large portion of the copper traces remain exposed only to oil. If the dielectric loss of the sample is small, then the input RF impedance will be very large, making impedance matching

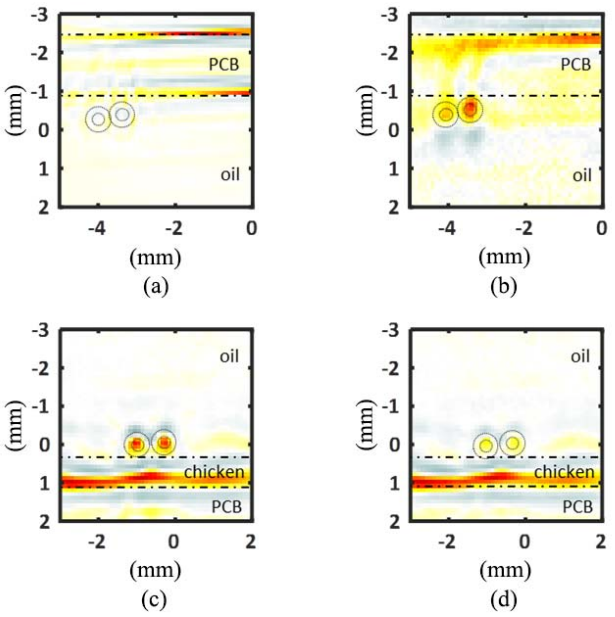

Fig. 10. (a) US and (b) TA image of two saline-filled Teflon microcapillaries. Saline concentration was increased to (c) 8× and (d) 4× with the addition of a layer of chicken skin under TA imaging.

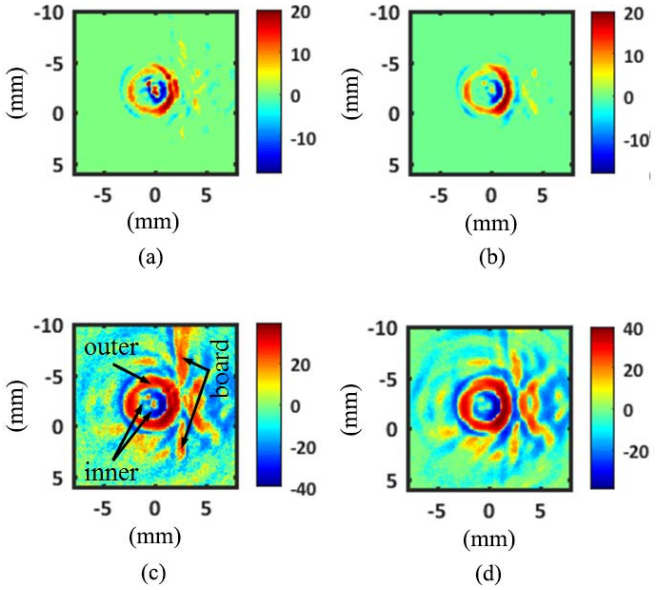

Fig. 11. TA imaging in log scale (dB) of two inner microcapillaries filled with (a) and (b) 8× normal saline and (c) and (d) 1× normal saline surrounded by an outer layer of (a) and (c) tap water or (b) and (d) 1× normal saline, with a maximum theoretical dynamic range of 40 dB.

impractical as it would limit bandwidth necessary to obtain sufficient resolution.

C. Results

The first step in the investigation of the TA imaging performance under circular scanning involved the simple, compact dipole RF applicator and an artificial vasculature phantom. Normal saline served as a blood phantom and was prepared by dissolving 3.6 g of table salt in 400 mL of tap water. The saline solution was injected into two Teflon microcapillaries with inner diameters of 280 μm and outer diameters of 640 μm as a proxy for blood vessels. The microcapillaries were positioned with 1.6 mm standoff from the copper traces on the dipole RF applicator. The resulting cross-sectional images obtained with conventional US and TA are shown in Fig. 10(a) and (b), respectively, which illustrate about 300 μm resolution after image reconstruction using a computation grid comprising 100-μm pixels. The details of the imaging and reconstruction processes are described in [47]. To create a more realistic phantom of the fingertip, 0.5 to 1 mm thick chicken skin was added. Here, a 100 μm layer of polyethylene terephthalate plastic insulated the two-trace PCB from the chicken skin, behind which the micro capillaries were situated. The salinity was increased by a factor of 8× and 4×, respectively, and cross-sectional images were obtained as in Fig. 10(c) and (d). The clear dependence of the signal strength on salinity demonstrates that the TA effect occurs inside the capillary rather than due to thermal expansion of the capillary itself. However, the Teflon capillary can impede the propagation of acoustic waves, as Teflon has an acoustic impedance of about 3 Mrayl compared with approximately 1.5 Mrayl for water, tissue, and oil. At high acoustic frequencies, reflections occur, as acoustic waves travel from the saline into the capillary wall and then again when these waves travel from the capillary wall into the oil medium. Thus, in total, a significant portion (as much as 89% at high frequencies) of the incidence wave may be impeded.

Microwave penetration into tissue is generally restricted due to losses within the skin. To quantify this effect, an earthworm phantom was created using two plastic tubings and two Teflon microcapillaries. The two microcapillaries were filled with saline and enclosed by the smaller plastic tubing, approximately 3 mm in diameter. This tubing was filled with mineral oil to emulate fat. An outer tubing covered this entire assembly and was filled with tap water or saline to emulate an outer layer of skin. Resulting images are shown in Fig. 11, where at most a 30 dB dynamic range is observed between the vascular phantom (microcapillaries) and the skin phantom (outer saline layer). This is in good agreement with typical observations from electromagnetic simulations. It should be noted that the artifacts are expected outside the region corresponding to the skin phantom (labeled as outer) due to background TA signals from the RF-applicator circuit board and acoustic reflections. Each pixel, q, in a given log-scaled image was obtained using

$$q = \mathrm{sgn}(p) \cdot \max\left(20\log_{10}\left(\frac{|p|}{\max(|p|)}\right) + \mathrm{DR},\ 0\right) \quad (11)$$

where p is the observed pressure change for that pixel, $\max(|p|)$ is the maximum observed pressure change magnitude in the entire image, DR is the spurious free dynamic range of the receiver chain, and $\mathrm{sgn}(p)$ is $+1$ for positive pressure changes and -1 for negative pressure changes in the pixel. The spurious free dynamic range of the measurement equipment was limited to a maximum of 40 dB.

Images of biological samples were also obtained using the circular scanning approach as a means of evaluating the natural contrast present in tissue as well as overcoming the

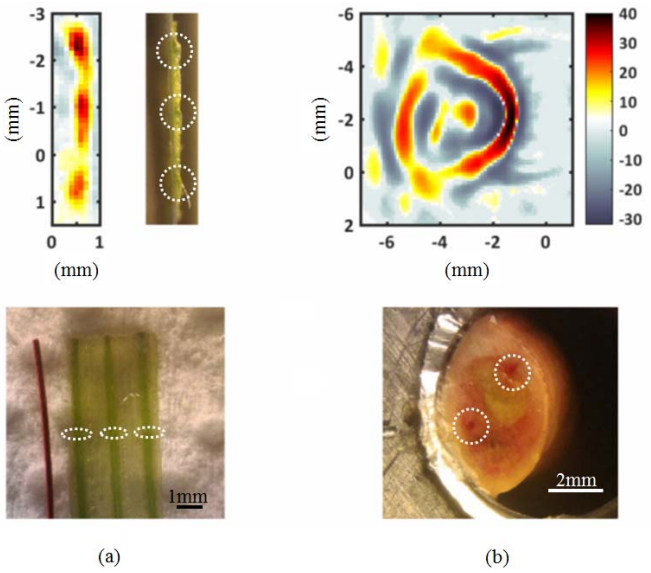

Fig. 12. TA imaging of (a) scallion plant with xylem comparable to a 260 μm diameter wire in linear scale and (b) earthworm showing inherent contrast between its two blood vessels and other tissue with log scaling.

acoustic impedance mismatch mentioned earlier. A sample of scallion plant and an earthworm, whose images are shown in Fig. 12, are ideal candidates as they can meet the small sample size requirement of the dipole RF applicator, as discussed previously. The scallion plant sample consisted of three vascular structures in the form of xylem and phloem pairs [65], comparable in size with a 260 μm diameter wire, that were slightly smaller than those reported in [47], where a leek plant was imaged instead. The TA image, in linear scale, reveals hotspots corresponding to these vessels, where water and electrolytes are more concentrated. Imaging of vasculature inside the earthworm is more challenging due to the outer layer of skin and muscle, which necessitates log scaling similar to Fig. 11. The earthworm was sacrificed with exposure to a tablespoon of isopropyl alcohol and was situated on the RF applicator. After TA imaging, the worm was carefully placed inside a plastic straw, which was then inserted into an aluminum block. This setup was frozen below 0 °C for 24 h. The setup was later quickly removed from the freezer and the worm sliced with a razor at the point corresponding to the imaging plane. The photograph of this cross section is in agreement with the TA image based on the two observed hotspots that corresponding to the dorsal and ventral blood vessels of the earthworm [66]. Due to the malleability of the worm, however, some deformation in the photograph is visible, which is attributed to the handling, freezing, and slicing process.

V. Raster Scanning and Results

So far, we have observed good performance of the TA circular scanning approach, in terms of SNR and resolution, similar to those demonstrated by [15]–[17] for PA. However, circular scanning is not feasible in the desired operating conditions of a TA-based biometric imager, as shown in Fig. 1.

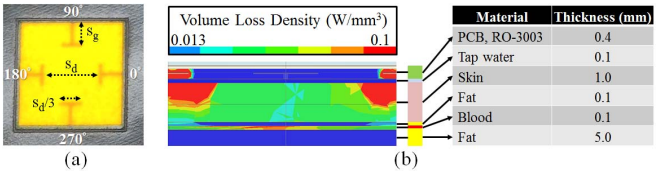

Material	Thickness (mm)
PCB, RO-3003	0.4
Tap water	0.1
Skin	1.0
Fat	0.1
Blood	0.1
Fat	5.0

Fig. 13. Zoomed-in view of (a) quadrupole RF applicator and (b) its corresponding simulation with a layered tissue model.

In addition, the simple dipole RF applicator is only effective on vasculature that is oriented into and out of the cross-sectional plane, hindering the imaging of more complex vascular structures. A more relevant method is the 2-D raster scanning of a focused commercial transducer, to synthetically create an equivalent 2-D phased-array transducer, together with a planar RF-applicator PCB designed for uniform illumination of multiple vessels with various independent orientations. While off-the-shelf focused transducers are not designed to achieve the desired lateral resolution, this will allow the evaluation of the RF-applicator's performance, which will be directly reflective of the ideal system in Fig. 1. We will now explore this approach, performed with the common experimental setup shown in Fig. 9.

A. Quadrupole RF-Applicator Design

While the microcapillaries and vasculature imaged with the circular scanning approach had identical and optimal orientation, the blood vessels of the finger have multiple independent orientations. In order to uniformly excite all vasculature in an orientation-independent manner, the applied electric field must ideally be polarized in all possible directions along the vasculature. One way to achieve this is to employ two sets of dipole electrodes arranged in the manner shown in Fig. 13(a), here on referred to as the quadrupole RF applicator. Each electrode of the quadrupole RF applicator is fed with a specific RF phase of 0°, 90°, 180°, and 270°, in order to form a circularly polarized electric field between the electrodes and within the sample. Consequently, the time-averaged electric field intensity is approximately constant in any direction parallel with plane of the PCB, and so the excitation of vessels is approximately uniform irrespective of their particular orientation.

The quadrupole applicator is designed to operate in both the low-permittivity and lossless mineral oil environment as well as the low-loss and high-permittivity environment of distilled or tap water. This is made possible, since the ground planes only expose a small region of interest around the quadrupole to the targeted lossy or high-permittivity materials. The spacing between quadrupoles, s_d, is 5 mm to give an optimal penetration depth of 3.5 mm according to (4), assuming a low-permittivity environment. This serves as a starting point for iterative design through simulation under high-permittivity environment, such as in water or tissue, which results in complex electrical behavior that is not fully modeled by the simple theory of (3) and (4).

The optimal spacing between the ground planes and the quadrupoles and the ideal operating frequency are determined

by simulation optimization in Ansoft HFSS using the tissue layer structure of skin, fat, and blood shown in Fig. 13(b). The frequency-dependent dielectric properties of this tissue are modeled based on collected data by [58]. These simulations revealed that optimal operating frequency corresponds to a wavelength that is approximately twice the quadrupole separation, s_d. Choosing a ground plane and quadrupole separation, s_g, of about a half-wavelength maximizes power delivered to the blood layer, while setting it to about a quarter-wavelength maximizes the ratio of the delivered power to the blood with respect to that delivered to skin. This is generally equal to or greater than the delivered optical power in an equivalent PA imaging system based on Monte Carlo simulations [67] for PA imaging using the layered-tissue model in [68]. Finally, the lossy properties of the skin permit RF impedance matching while maintaining sufficient bandwidth ($\geq$20 MHz) for image resolution. Electromagnetic simulations and experimental results on the earthworm suggest up to four times improvement in TA signals after matching.

B. Experimental Setups

Each electrode of the quadrupole RF applicator was fed with its corresponding RF phase through an SMA connector and a stripline transmission line. This proof-of-concept system used commercial 90° and 180° hybrid couplers to generate the necessary RF phases of 0°, 90°, 180°, and 270°, from the single-port output of the circulator in Fig. 9. Considering that the subcutaneous vasculature of interest is a few millimeters beneath the skin, and that during an imaging procedure the finger would press flat against a planar RF-applicator PCB, a 2D microfluidic network of multidirectional channels serves as a good model of this geometry. As discussed earlier in the theory, resolution will decrease if a bulky (i.e., commercial) planar transducer, or an off-the-shelf focused device, is used as a substitute for an MEMS transducer or phased array. Consequently, a microfluidic structure consisting of 300 μm wide channels spaced several millimeters apart in various orientations was made. The 2D microfluidic pattern, with exposed channels, was 3D printed using multijet modeling technology. A silicone mold of this pattern was made, into which Polyester Casting Resin was poured. After 48 h of curing, the polyester piece contained grooves, which were then sealed with clear 3M Scotch Tape to form microfluidic channels. Teflon microcapillaries were epoxied at the inlet and outlet to form a complete microfluidic device. Since these materials have very low dielectric loss, relatively low levels of TA signals are generated unless saline is present inside the channels.

C. Excitation Uniformity Results

The generation of the four required RF phases will inevitably be imperfect, as there will be phase and gain mismatch between them, leading to production of elliptical rather than circular electric field polarization. This contributes to degradation of excitation uniformity, which was measured using a saline-filled, single-channel microfluidic structure, as shown in Fig. 14. The channel was aligned with one pair

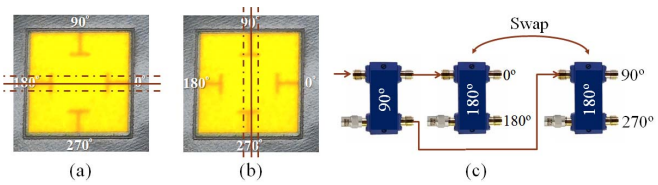

Fig. 14. Measurement of the RF-excitation along (a) x-axis and (b) y-axis of the RF applicator with an aligned, saline-filled microcapillary. The microcapillary was repositioned to find the US transducer's focal point. The hybrid couplers producing the four RF phases were (c) swapped to evaluate their contribution to excitation nonuniformity.

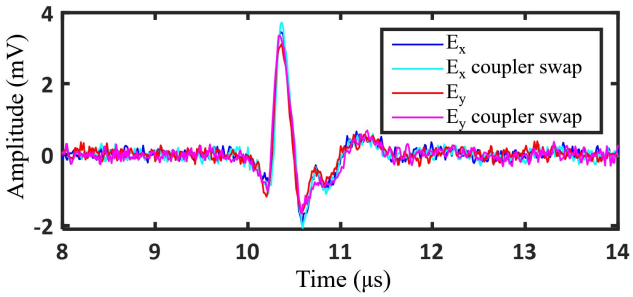

Fig. 15. Saline-filled microfluidic channel was aligned with the x-axis, and subsequently y-axis, electrode pairs of the quadrupole RF applicator. The TA signals showed no more than 10% variation.

of the four quadrupoles, i.e., along the x-axis, and the time-domain TA signal was observed. The microfluidic structure was swept along the perpendicular y-axis in order to locate the focus of the transducer, which does not necessarily align with the quadrupole center. This was repeated for the other pair of electrodes along the y-axis. Finally, this entire process was performed again after swapping the outputs of the hybrid couplers that fed the quadrupole RF applicator, to obtain the recorded TA signals shown in Fig. 15.

Referring to Fig. 15, it is observed that the transducer focus misalignment was greater along the y-axis, which explains the consistently weaker TA signal from the y-axis electrode pairs. The total RF gain and phase mismatch among the four ports was characterized by a vector-network analyzer to 8% and 7°, respectively. As observed in Fig. 15, the 10% uniformity mismatch, U, is below the specified 20% variation, where

$$U = \begin{cases} \dfrac{\mathrm{TA}_x - \mathrm{TA}_y}{\mathrm{TA}_x}, & \text{if } \mathrm{TA}_x > \mathrm{TA}_y \\ \dfrac{\mathrm{TA}_y - \mathrm{TA}_x}{\mathrm{TA}_y}, & \text{if } \mathrm{TA}_x < \mathrm{TA}_y. \end{cases} \tag{12}$$

This quantity can be converted to an equivalent eccentricity of 0.32 for the elliptically polarized electric field, considering that the TA signal is proportional to the square magnitude of the electric field. The eccentricity, e, can be described as

$$e = \begin{cases} \sqrt{1 - \left(\dfrac{E_y}{E_x}\right)^2}, & \text{if } E_x > E_y \\ \sqrt{1 - \left(\dfrac{E_x}{E_y}\right)^2}, & \text{if } E_x < E_y \end{cases} \tag{13}$$

where E_x is the magnitude of the electric field generated by the pair of electrodes along the x-axis and E_y is similar

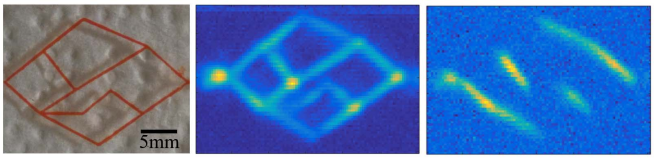

(a) (b) (c)

Fig. 16. TA imaging of (a) saline-filled 2-D microfluidic structure using the quadrupole RF applicator with (b) four electrodes and RF phases activated or (c) only two electrodes activated.

TABLE I
SPECIFICATIONS MET BY EXPERIMENTS

Experiment	SNR	Contrast	Resolution	Depth	Uniformity
Microcapillaries	✓	∼	✓	∼	×
Microcap.+Skin	∼	✓	✓	✓	×
Scallion	✓	✓	✓	∼	×
Earthworm	✓	✓	∼	✓	×
2D Microfluidics	✓	∼	×	∼	✓

for the y-axis. In summary, successful TA imaging of complex vascular structures such as those in the finger will necessitate excitation uniformity, with respect to electric field orientations, and the proposed quadruple RF applicator is capable of meeting this demand.

D. Imaging Results

A raster scanning setup similar to Fig. 9, employing a focused transducer (Olympus Parametric C308) and quadrupole RF applicator, was used to obtain the TA images of the saline-filled 2D microfluidic structure in Fig. 16(a), under both four-electrode excitation and two-electrode excitation, respectively. As expected, the four electrodes produced circularly polarized electric fields in the sample, when each port is driven with the proper RF phase, creating a symmetric excitation that results in the desired image of Fig. 16(b). On the other hand, when only two electrodes are activated, similar to the simple dipole RF applicator, a linear polarization is formed that only illuminates channels, which are aligned with the linear orientation, resulting in the undesirable image of Fig. 16(c). Finally, while the results obtained in Fig. 16 are limited to a resolution of 1.2 mm or larger, due to the $\geq$ 0.6-mm beamwidth of the commercial focused transducer, this will improve with an MEMS transducer array.

VI. DISCUSSION

The experimental results obtained with circular and raster scanning of a single transducer can now be used to predict the feasibility and performance of the proposed, ideal TA biometric imaging system in Fig. 1. In addition, areas of improvement can be identified for future work.

Referring to Table I, we can see that the cross-sectional imaging of the earthworm with the circular scanning approach met the most important specifications: SNR, contrast, and sufficient penetration depth. Since the worm's blood vessels were 0.5 mm or larger, it does not serve as a good measure of resolution, which was confirmed by other experiments on the microcapillaries. The limiting factor so far has been the 40 dB minimum receiver dynamic range required to successfully image subcutaneous vasculature, which is still more lenient than the 70 to 120 dB requirements found in conventional Doppler US and vector-velocity US imaging techniques [69]–[72]. Thus, all specifications outlined earlier in this paper are currently satisfied with the exception of the power and acquisition time requirements.

In order to further improve the resolution as well as reduce acquisition time, a TA-based biometric imager system would need to employ transducers arrays and application-specific front-end electronics similar to [73]–[75]. For example, a 1 cm $\times$ 1 cm 2-D array made up of 75 μm $\times$ 75 μm elements similar to the 1-D array reported in [73] is expected to have an NEP of 0.43 Pa, averaged over the array. This is slightly higher than the 0.2-Pa NEP of the synthetic aperture formed by the V320 after circular scanning. To meet the SNR specifications, based on experimental observations in Fig. 12, we would require at least 50 averages to reduce the NEP to 0.06 Pa. With 32 receive channels in the front end, the image acquisition can be performed within 3 s. To further reduce the power down to levels compatible with mobile devices, CW techniques, such as those reported in [34] and [35], may have to be used.

Prior works in TA imaging demonstrate 1 mm typical resolution within a range of 0.1–4 mm, as well as typical peak and average powers of 10 kW and 16 W within a range of 20 kW–70 MW and 60 mW–70 W, respectively [26]–[33], [36], [43]. By customizing our TA imaging implementation for superficial vasculature of the fingertip, we have obtained a better resolution, 0.3 mm, as well as the lowest peak power, at 50 W, and average power at 42 mW. In comparison, PA imaging works in the literature typically demonstrate between 0.1 and 0.5 mm resolution when acoustically focused and down to several micrometers when optically focused using more than 100 kW of peak power and 200 mW average power corresponding to the 20 mJ/pulse laser safety limit and a typical 20 Hz pulse rate [10]–[12], [14]–[21].

VII. CONCLUSION

In this paper, we highlighted the potential of the TA imaging modality as a safe, cost-effective, low-power, and compact method for capturing biometric features from subcutaneous vasculature. Despite the drastic power reductions compared with conventional implementations of TA imaging, we show that sufficient SNR can be attained by increasing microwave excitation uniformity and concentrating it in the near field and quasi-near field by an optimized RF-applicator design. Heuristic methods are outlined to inform this design process, which can be further optimized in simulation. Finally, we used theory, simulations, and data from proof-of-concept experiments to more accurately interpret the performance of these RF applicators in order to assess viability of TA imaging for biometrics on mobile and wearable platforms. Analysis of experiments, simulations, and theory suggests the possibility of further improvement using MEMS US arrays, including enhanced resolution down to 150 μm and reduced image acquisition time from 10 min to a few seconds. All-in-all, the results support the feasibility of this application and encourage the development of a prototype as a future work.

ACKNOWLEDGMENT

This work was supported in part by the Qualcomm Innovation Fellowship program, the Texas Instruments University Relations Program, and the Stanford System-X Alliance. The authors appreciate the assistance of RFMD and Rhode & Schwarz in procuring laboratory resources and are grateful to Prof. Khuri-Yakub, Dr. Nemat Dolatsha, and Dr. Nikoozadeh from Stanford University for their enlightening suggestions and discussions.

REFERENCES

[1] D. Hartung, "Vascular pattern recognition: And its application in privacy-preserving biometric online-banking systems," Ph.D. dissertation, Dept. Comput. Sci. Media Technol., Gjøvik Univ. College, Trondheim, Norway, 2012.

[2] B. Zabihian *et al.*, "*In vivo* dual-modality photoacoustic and optical coherence tomography imaging of human dermatological pathologies," *Biomed. Opt. Exp.*, vol. 6, no. 9, pp. 3163–3178, 2015.

[3] A. Alex *et al.*, "Multispectral *in vivo* three-dimensional optical coherence tomography of human skin," *J. Biomed. Opt.*, vol. 15, no. 2, pp. 026025-1–026025-15, 2010.

[4] K. Cao and A. K. Jain, "Hacking mobile phones using 2D printed fingerprints," Michigan State Univ., East Lansing, MI, USA, Tech. Rep., 2016. [Online]. Available: http://www.cse.msu.edu/rgroups/biometrics/Publications/Fingerprint/CaoJain_HackingMobilePhonesUsing2DPrintedFingerprint_MSU-CSE-16-2.pdf

[5] K. Barlinn and A. V. Alexandrov, "Vascular imaging in stroke: Comparative analysis," *Neurotherapeutics*, vol. 8, no. 3, pp. 340–348, 2011.

[6] R. C. Gessner, C. B. Frederick, F. S. Foster, and P. A. Dayton, "Acoustic angiography: A new imaging modality for assessing microvasculature architecture," *J. Biomed. Imag.*, vol. 2013, pp. 14-1–14-9, Jun. 2013.[Online]. Available: https://www.hindawi.com/journals/ijbi/2013/936593/

[7] R. C. Preston, *Output Measurements for Medical Ultrasound*. London, U.K.: Springer, 1991.

[8] U. Baran, L. Shi, and R. K. Wang, "Capillary blood flow imaging within human finger cuticle using optical microangiography," *J. Biophoton.*, vol. 8, nos. 1–2, pp. 46–51, 2013.

[9] A. G. Bell, "Upon the production and reproduction of sound by light," *J. Soc. Telegraph Eng.*, vol. 9, no. 34, pp. 404–426, 1880.

[10] J. Xia, J. Yao, and L. V. Wang, "Photoacoustic tomography: Principles and advances," *Electromagn. Waves*, vol. 147, pp. 1–22, Jan. 2014.

[11] L. V. Wang, "Tutorial on photoacoustic microscopy and computed tomography," *IEEE J. Sel. Topics Quantum Electron.*, vol. 14, no. 1, pp. 171–179, Jan. 2008.

[12] J. Yao and L. V. Wang, "Sensitivity of photoacoustic microscopy," *Photoacoustics*, vol. 2, no. 2, pp. 87–101, 2014.

[13] S. Hu and L. V. Wang, "Photoacoustic imaging and characterization of the microvasculature," *J. Biomed. Opt.*, vol. 15, no. 1, pp. 011101-1–011101-15, 2010.

[14] E. Zhang, J. G. Laufer, R. B. Pedley, and P. C. Beard, "*In vivo* high-resolution 3D photoacoustic imaging of superficial vascular anatomy," *Phys. Med. Biol.*, vol. 54, no. 4, pp. 1035–1046, 2009.

[15] E. P. van Vlieg *et al.*, "Coregistered photoacoustic and ultrasound tomography of healthy and inflamed human interphalangeal joints," in *Proc. Eur. Conf. Biomed. Opt.*, 2015, pp. 95390C-1–95390C-6.

[16] Z. Deng and C. Li, "Noninvasively measuring oxygen saturation of human finger-joint vessels by multi-transducer functional photoacoustic tomography," *J. Biomed. Opt.*, vol. 21, no. 6, pp. 061009-1–061009-5, 2016.

[17] L. Xi and H. Jiang, "High resolution three-dimensional photoacoustic imaging of human finger joints *in vivo*," *Appl. Phys. Lett.*, vol. 107, no. 6, pp. 063701-1–063701-3, 2015.

[18] K. Maslov and L. V. Wang, "Photoacoustic imaging of biological tissue with intensity-modulated continuous-wave laser," *J. Biomed. Opt.*, vol. 13, no. 2, pp. 024006-1–024006-5, 2008.

[19] L. Zeng, G. Liu, D. Yang, and X. Ji, "Portable optical-resolution photoacoustic microscopy with a pulsed laser diode excitation," *Appl. Phys. Lett.*, vol. 102, no. 5, pp. 053704-1–053704-4, 2013.

[20] B. Lashkari and A. Mandelis, "Linear frequency modulation photoacoustic radar: Optimal bandwidth and signal-to-noise ratio for frequency-domain imaging of turbid media," *J. Acoust. Soc. Amer.*, vol. 130, no. 3, pp. 1313–1324, 2011.

[21] K. Maslov, H. F. Zhang, S. Hu, and L. V. Wang, "Optical-resolution photoacoustic microscopy for *in vivo* imaging of single capillaries," *Opt. Lett.*, vol. 33, no. 9, pp. 929–931, 2008.

[22] K. Sivasubramanian and M. Pramanik, "High frame rate photoacoustic imaging at 7000 frames per second using clinical ultrasound system," *Biomed. Opt. Exp.*, vol. 7, no. 2, pp. 312–323, 2016.

[23] S.-Y. Su and P.-C. Li, "Coded excitation for photoacoustic imaging using a high-speed diode laser," *Opt. Exp.*, vol. 19, no. 2, pp. 1174–1182, 2011.

[24] L. V. Wang, *Photoacoustic Imaging and Spectroscopy*. Boca Raton, FL, USA: CRC Press, 2009.

[25] C. Hoelen and F. De Mul, "A new theoretical approach to photoacoustic signal generation," *J. Acoust. Soc. Amer.*, vol. 106, no. 2, pp. 695–706, 1999.

[26] Y. Xu and L. V. Wang, "Rhesus monkey brain imaging through intact skull with thermoacoustic tomography," *IEEE Trans. Ultrason., Ferroelect., Freq. Control*, vol. 53, no. 3, pp. 542–548, Mar. 2006.

[27] R. A. Kruger *et al.*, "Thermoacoustic CT with radio waves: A medical imaging paradigm 1," *Radiology*, vol. 211, no. 1, pp. 275–278, 1999.

[28] R. Kruger, W. L. Kiser, D. R. Reinecke, G. A. Kruger, and R. L. Eisenhart, "Thermoacoustic computed tomography of the breast at 434 MHz," in *IEEE MTT-S Int. Microw. Symp. Dig.*, vol. 2. Jun. 1999, pp. 591–594.

[29] S. K. Patch *et al.*, "Toward quantitative whole organ thermoacoustics with a clinical array plus one very low-frequency channel applied to prostate cancer imaging," *IEEE Trans. Ultrason., Ferroelect., Freq. Control*, vol. 63, no. 2, pp. 245–255, Feb. 2016.

[30] Z. Ji, W. Ding, F. Ye, and C. Lou, "Handheld thermoacoustic scanning system based on a linear-array transducer," *Ultrason. Imag.*, vol. 38, no. 4, pp. 276–284, 2016.

[31] H. Lin *et al.*, "Thermoacoustic imaging of human finger joints and bones," *X-Acoust., Imagi. Sens.*, vol. 1, no. 1, pp. 28–31, 2015.

[32] F. Ye, Z. Ji, W. Ding, C. Lou, S. Yang, and D. Xing, "Ultrashort microwave-pumped real-time thermoacoustic breast tumor imaging system," *IEEE Trans. Med. Imag.*, vol. 35, no. 3, pp. 839–844, Mar. 2016.

[33] C. Lou, S. Yang, Z. Ji, Q. Chen, and D. Xing "Ultrashort microwave-induced thermoacoustic imaging: A breakthrough in excitation efficiency and spatial resolution," *Phys. Rev. Lett.*, vol. 109, no. 21, p. 218101, 2012.

[34] X. Wang and Y. Liu, "Frequency domain continuous-wave microwave induced thermoacoustic tomography," in *Proc. IEEE 13th Int. Symp. Biomed. Imag. (ISBI)*, Jul. 2016, pp. 714–717.

[35] H. Nan and A. Arbabian, "Coherent frequency-domain microwave-induced thermoacoustic imaging," in *IEEE MTT-S Int. Microw. Symp. Dig.*, Oct. 2014, pp. 1–4.

[36] H. Nan and A. Arbabian, "Peak-power-limited frequency-domain microwave-induced thermoacoustic imaging for handheld diagnostic and screening tools," *IEEE Trans. Microw. Theory Techn.*, to be published.

[37] H. Nan, S. Liu, N. Dolatsha, and A. Arbabian, "A 16-element wideband microwave applicator for breast cancer detection using thermoacoustic imaging," in *Proc. PIERS*, 2015, pp. 243–247.

[38] X. Wang, D. R. Bauer, J. L. Vollin, D. G. Manzi, R. S. Witte, and H. Xin, "Impact of microwave pulses on thermoacoustic imaging applications," *IEEE Antennas Wireless Propag. Lett.*, vol. 11, pp. 1634–1637, 2012.

[39] K. C. Boyle, H. Nan, B. T. Khuri-Yakub, A. Arbabian, "Non-contact thermoacoustic detection of targets embedded in dispersive media," *Proc. SPIE*, vol. 9988, pp. 99880H-1–99880H-7, Oct. 2016. [Online]. Available: http://proceedings.spiedigitallibrary.org/proceeding.aspx?articleid=2575600

[40] G. Alexopoulos, K. C. Boyle, N. Dolatsha, H. Nan, B. T. Khuri-Yakub, and A. Arbabian, "Standoff tracking of medical interventional devices using non-contact microwave thermoacoustic detection," in *IEEE MTT-S Int. Microw. Symp. Dig.*, May 2016, pp. 1–4.

[41] H. Nan *et al.*, "Non-contact thermoacoustic detection of embedded targets using airborne-capacitive micromachined ultrasonic transducers," *Appl. Phys. Lett.*, vol. 106, no. 8, pp. 084101-1–084101-4, 2015.

[42] K. C. Boyle *et al.*, "Non-contact thermoacoustic imaging of tissue with airborne ultrasound detection," in *Proc. IEEE Int. Ultrason. Symp. (IUS)*, Oct. 2015, pp. 1–4.

[43] S. Kellnberger, A. Hajiaboli, D. Razansky, and V. Ntziachristos, "Near-field thermoacoustic tomography of small animals," *Phys. Med. Biol.*, vol. 56, no. 11, pp. 3433–3444, 2011.

[44] X. Feng, F. Gao, and Y. Zheng, "Magnetically mediated thermoacoustic imaging," *Proc. SPIE*, vol. 8943, pp. 894343-1–894343-4, Mar. 2014. [Online]. Available: http://proceedings.spiedigitallibrary.org/proceeding.aspx?articleid=1840475

[45] S. Kellnberger, M. Omar, G. Sergiadis, and V. Ntziachristos, "Second harmonic acoustic responses induced in matter by quasi continuous radiofrequency fields," *Appl. Phys. Lett.*, vol. 103, no. 15, pp. 153706-1–153706-4, 2013.
[46] A. Ahlbom, "Guidelines for limiting exposure to time-varying electric, magnetic, and electromagnetic fields (up to 300 GHz)," *Health Phys.*, vol. 74, no. 4, pp. 494–521, 1998.
[47] M. Aliroteh *et al.*, "Microwave-induced thermoacoustic tomography for subcutaneous vascular imaging," in *Proc. IEEE Int. Ultrason. Symp. (IUS)*, May 2016, pp. 1–4.
[48] H. Nan, B. A. Haghi, and A. Arbabian, "Interferogram-based breast tumor classification using microwave-induced thermoacoustic imaging," in *Proc. 37th Annu. Int. Conf. IEEE Eng. Med. Biol. Soc. (EMBC)*, Dec. 2015, pp. 2717–2720.
[49] L. Yao, G. Guo, and H. Jiang, "Quantitative microwave-induced thermoacoustic tomography," *Med. Phys.*, vol. 37, no. 7, pp. 3752–3759, 2010.
[50] G. Bal, K. Ren, G. Uhlmann, and T. Zhou, "Quantitative thermoacoustics and related problems," *Inverse Problems*, vol. 27, no. 5, pp. 055007-1–055007-15, 2011.
[51] S. Curto, "Antenna development for radio frequency hyperthermia applications," Ph.D. dissertation, Dept. Electron. Commun. Eng., Dublin Inst. Technol., Dublin, Ireland, 2016. [Online]. Available: http://arrow.dit.ie/engdoc/38/
[52] W. Kester, "Taking the mystery out of the infamous formula, 'SNR = 6.02N + 1.76dB,' and why you should care," Analog Devices Inc., Greensboro, NC, USA, Tech. Rep. MT-001 Tutorial, 2009. [Online]. Available: http://www.analog.com/static/imported-files/tutorials/MT-001.pdf
[53] M. Fioreze, S. dos S. Junior, and M. G. Hönnicke, "Can we estimate the cellular phone RF peak output power with a simple experiment?" *Eur. J. Phys.*, vol. 37, no. 4, pp. 045801-1–045801-12, 2016.
[54] N. Vidal, J. M. López-Villegas, "Changes in electromagnetic field absorption in the presence of subcutaneous implanted devices: Minimizing increases in absorption," *IEEE Trans. Electromagn. Compat.*, vol. 52, no. 3, pp. 545–555, Mar. 2010.
[55] A. Christ, T. Samaras, A. Klingenböck, and N. Kuster, "Characterization of the electromagnetic near-field absorption in layered biological tissue in the frequency range from 30 MHz to 6000 MHz," *Phys. Med. Biol.*, vol. 51, no. 19, p. 4951, 2006.
[56] E. Alanen, T. Lahtinen, and J. Nuutinen, "Penetration of electromagnetic fields of an open-ended coaxial probe between 1 MHz and 1 GHz in dielectric skin measurements," *Phys. Med. Biol.*, vol. 44, no. 7, p. N169, 1999.
[57] P. J. Riu and K. R. Foster, "Heating of tissue by near-field exposure to a dipole: A model analysis," *IEEE Trans. Biomed. Eng.*, vol. 46, no. 8, pp. 911–917, Aug. 1999.
[58] D. Andreuccetti, R. Fossi, and C. Petrucci, "An Internet resource for the calculation of the dielectric properties of body tissues in the frequency range 10 Hz–100 GHz," *Inst. Appl. Phys.*, to be published. [Online]. Available: http://niremf.ifac.cnr.it/tissprop/
[59] X. C. Jin, B. T. Ehuri-Yakub, F. L. Degertekin, I. Ladabaum, and S. Calmes, "Micromachined capacitive ultrasonic immersion transducer for medical imaging," in *Proc. 20th Annu. Int. Conf. IEEE Eng. Med. Biol. Soc.*, vol. 2. Oct. 1998, pp. 779–782.
[60] D. Zhao *et al.*, "A commercialized high frequency CMUT probe for medical ultrasound imaging," in *Proc. IEEE Int. Ultrason. Symp. (IUS)*, 2015, pp. 1–4.
[61] A. S. Savoia, G. Caliano, and M. Pappalardo, "A CMUT probe for medical ultrasonography: From microfabrication to system integration," *IEEE Trans. Ultrason., Ferroelect., Freq. Control*, vol. 59, no. 6, pp. 1127–1138, Jun. 2012.
[62] M. H. Skjelvareid, "Synthetic aperture ultrasound imaging with application to interior pipe inspection," Ph.D. dissertation, Dept. Phys. Technol., Univ. Tromsø, Tromsø, Norway, 2012. [Online]. Available: https://core.ac.uk/download/pdf/19640369.pdf
[63] D. M. Sheen, D. L. McMakin, and T. E. Hall, "Three-dimensional millimeter-wave imaging for concealed weapon detection," *IEEE Trans. Microw. Theory Techn.*, vol. 49, no. 9, pp. 1581–1592, Sep. 2001.
[64] B. E. Treeby and B. T. Cox, "k-Wave: Matlab toolbox for the simulation and reconstruction of photoacoustic wave fields," *J. Biomed. Opt.*, vol. 15, no. 2, p. 021314-1–021314-12, 2010.
[65] J. L. Brewster, *Onions and Other Vegetable Alliums*. Oxfordshire, U.K.: CABI, 2008, pp. 1–22.
[66] C. A. Edwards and P. J. Bohlen, *Biology and Ecology of Earthworms*, vol. 3. London, U.K.: Springer, 1996.
[67] Q. Fang and D. A. Boas, "Monte Carlo simulation of photon migration in 3D turbid media accelerated by graphics processing units," *Opt. Exp.*, vol. 17, no. 22, pp. 20178–20190, 2009.
[68] O. Kim, J. McMurdy, C. Lines, S. Duffy, G. Crawford, and M. Alber, "Reflectance spectrometry of normal and bruised human skins: Experiments and modeling," *Physiol. Meas.*, vol. 33, no. 2, pp. 159–175, 2012.
[69] J. A. Jensen *et al.*, "Ultrasound research scanner for real-time synthetic aperture data acquisition," *IEEE Trans. Ultrason., Ferroelect., Freq. Control*, vol. 52, no. 5, pp. 881–891, May 2005.
[70] D. A. Christopher, P. N. Burns, B. G. Starkosk, F. S. Foster, "A high-frequency pulsed-wave doppler ultrasound system for the detection and imaging of blood flow in the microcirculation," *Ultrasound Med. Biol.*, vol. 23, no. 7, pp. 997–1015, 1997.
[71] C. H. Seo and J. T. Yen, "Sidelobe suppression in ultrasound imaging using dual apodization with cross-correlation," *IEEE Trans. Ultrason., Ferroelect., Freq. Control*, vol. 55, no. 10, pp. 2198–2210, Oct. 2008.
[72] D. Lieu, "Ultrasound physics and instrumentation for pathologists," *Arch. Pathol. Lab. Med.*, vol. 134, no. 10, pp. 1541–1556, 2010.
[73] K. K. Park, O. Oralkan, and B. T. Khuri-Yakub, "A comparison between conventional and collapse-mode capacitive micromachined ultrasonic transducers in 10-MHz 1-D arrays," *IEEE Trans. Ultrason., Ferroelect., Freq. Control*, vol. 60, no. 6, pp. 1245–1255, Jun. 2013.
[74] I. O. Wygant *et al.*, "Integration of 2D CMUT arrays with front-end electronics for volumetric ultrasound imaging," *IEEE Trans. Ultrason., Ferroelect., Freq. Control*, vol. 55, no. 2, pp. 327–342, Feb. 2008.
[75] P. Cristman *et al.*, "A 2D CMUT hydrophone array: Characterization results," in *Proc. IEEE Int. Ultrason. Symp. (IUS)*, Jun. 2009, pp. 992–995.

Miaad S. Aliroteh (S'13) received the B.A.Sc. degree (Hons.) in engineering science (with a major in electrical and computer engineering) from the University of Toronto, Toronto, ON, Canada, in 2012. He is currently pursuing the Ph.D. degree in electrical engineering at Stanford University, Stanford, CA, USA.

His current research interests include multimodal imaging, biometrics, biosensing and diagnostics, neural interfaces, wireless implantable or wearable devices, and analog and RF VLSI.

Mr. Aliroteh was the recipient of the PGS M Scholarship from the Natural Sciences and Engineering Research Council of Canada in 2012 and the Qualcomm Innovation Fellowship in 2014.

Amin Arbabian (S'06–M'12) received the Ph.D. degree in electrical engineering and computer science from the University of California at Berkeley (UC Berkeley), Berkeley, CA, USA, in 2011.

In 2007 and 2008, he was part of the Initial Engineering Team, Tagarray, Inc., Palo Alto, CA, USA. He was with the Qualcomm's Corporate Research and Development Division, in 2010, where he designed circuits for next-generation ultralow-power wireless transceivers. In 2012, he joined Stanford University, Stanford, CA, USA, as an Assistant Professor of electrical engineering, where he is currently a School of Engineering Frederick E. Terman Fellow. His current research interests include high-frequency circuits, systems, and antennas, medical imaging, and ultralow power sensors.

Dr. Arbabian was a recipient or a co-recipient of the 2015 NSF CAREER Award, the 2014 DARPA Young Faculty Award, the 2013 IEEE International Conference on Ultra-Wideband Best Paper Award, the 2013 Hellman Faculty Scholarship, the 2010 IEEE Jack Kilby Award for Outstanding Student Paper of the International Solid-State Circuits Conference, two-time Second Place Best Student Paper Award at the 2008 and 2011 Radio-Frequency Integrated Circuits (RFIC) Symposium, the 2009 Center for Information Technology Research in the Interest of Society at UC Berkeley Big Ideas Challenge Award and the UC Berkeley Bears Breaking Boundaries Award, and the 2010–2011 and 2014–2015 Qualcomm Innovation Fellowship. He currently serves on the TPC for the European Solid-State Circuits Conference and the RFIC Symposium.